

Article

Picosecond Photoacoustic Metrology of SiO₂ and LiNbO₃ Layer Systems Used for High Frequency Surface-Acoustic-Wave Filters

Delia Brick ^{1,*} , Erkan Emre ¹, Martin Grossmann ¹, Thomas Dekorsy ^{1,2} and Mike Hettich ¹

¹ Department of Physics, University of Konstanz, 78464 Konstanz, Germany; erkan.emre@uni-konstanz.de (E.E.); martin.grossmann@uni-konstanz.de (M.G.); thomas.dekorsy@uni-konstanz.de (T.D.); mike.hettich@uni-konstanz.de (M.H.)

² Institute of Technical Physics, German Aerospace Center, Pfaffenwaldring 38-40, 70569 Stuttgart, Germany

* Correspondence: delia.brick@uni-konstanz.de; Tel.: +49-7531-88-4911

Received: 7 July 2017; Accepted: 7 August 2017; Published: 10 August 2017

Abstract: Many applications of thin films necessitate detailed information about their thicknesses and sound velocities. Here, we study SiO₂/LiNbO₃ layer systems by picosecond photoacoustic metrology and measure the sound velocities of the respective layers and the film thickness of SiO₂, which pose crucial information for the fabrication of surface-acoustic-wave filters for communication technology. Additionally, we utilize the birefringence and the accompanying change in the detection sensitivity of coherent acoustic phonons in the LiNbO₃ layer to infer information about the LiNbO₃ orientation and the layer interface.

Keywords: picosecond photoacoustic metrology; LiNbO₃; SiO₂; surface-acoustic-wave filters

1. Introduction

Thin film technology forms the core of current semiconductor industries. One important sector is the fabrication and development of electro-acoustic filters often used in modern mobile phones [1,2]. Many applications require an exact knowledge of film thicknesses in the nanometer range, as well as their respective sound velocities which depend on the strain inside the films. Here, we present an approach to measure both quantities simultaneously by means of time-resolved photoacoustic spectroscopy [3,4] in thin SiO₂ films. This method has already been employed for measurements in similar systems, although without birefringent layers [5]. We additionally show that the polarization-dependent detection in LiNbO₃ can be utilized to reveal information about the LiNbO₃ crystal orientation and the SiO₂/LiNbO₃ interface [6–8]. This approach can also be applied to characterize a variety of further complex layer systems based on e.g., birefringent polymers [9], nanocomposites [10], or indium tin oxide (ITO)-based [11] devices. In addition, newly emerging materials, e.g., nanowire-based assemblies [12,13] exhibiting strong birefringence could be interesting to study from a more fundamental research point of view.

2. Materials and Methods

The structure of the investigated sample is depicted in the inset of Figure 1. It is composed of four layers, from bottom to top, i.e., 100-nm aluminium prepared by thermal evaporation (the Al layer is used in subsequent lithography steps in industrial applications), 325- μ m lithium niobate, and 1140-nm silicon dioxide prepared by reactive direct current-pulsed magnetron sputtering in addition to radio frequency bias on the substrate holder. The fourth layer is a chromium layer with a thickness of 18 nm, which is used as a transducer on top of the sample in order to generate the photoacoustic signal through pulsed laser excitation.

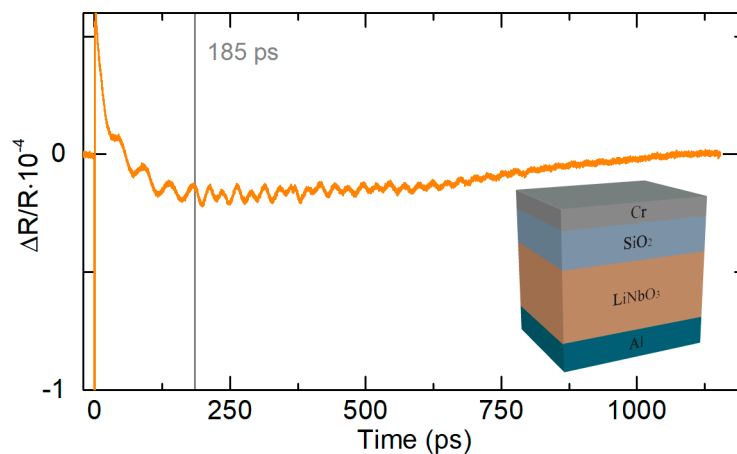


Figure 1. Transient reflectivity changes of the sample. Inset: Sample structure; from top to bottom, the sample consists of a layer of 18-nm Cr, 1140-nm SiO₂, 325- μ m LiNbO₃, and 100-nm Al (thicknesses are not to scale).

We use high-speed asynchronous optical sampling (ASOPS), a femtosecond time-resolved pump-probe technique [14–16], to perform the experiments. Two mode-locked femtosecond Ti:sapphire lasers (Gigajet Twin series, Laser Quantum GmbH, Konstanz, Germany), operating at 800 MHz, generate the pump and the probe pulse, respectively, with a stabilized offset of the repetition rates of 5 kHz. A 50 \times near infrared microscope objective (Mitutoyo, Sakado, Japan) was used to focus the laser beams to a spot size on the sample of about 2 μ m. The experiments were performed in a collinear setup in reflection geometry. Pump and probe powers were about 18 mW and 3 mW and the wavelengths were 790 nm and 820 nm, respectively.

3. Results and Discussion

The sample is excited from the Cr film side. In Figure 1, a typical transient of the reflectivity change $\Delta R/R$ after the optical excitation is shown.

A strong response in the first few tens of picoseconds is visible, which is caused by the fast electronic response in the Cr film [17–19]: the short laser pulse excites hot electrons inside the optoacoustic metal transducer which transfer their excess energy to the lattice via electron-phonon scattering. This process generates an impulsive strain pulse in the Cr film which propagates with the longitudinal speed of sound through the layer structure. Through the semi-transparent Cr film, the propagating strain pulse is monitored. Partially reflected probe light from the strain pulse is the origin of the associated change in the refractive index. This light interferes with the light being reflected from the top of the sample, giving rise to so-called time-resolved Brillouin oscillations with frequencies corresponding to the speed of sound in the material [20]. The acoustic pulse causes a small variation of the local index of refraction, which in turn results in a small portion of the probe light to be reflected at this position. Due to interference of the reflected light from the travelling pulse and the static sample interfaces, an oscillatory behavior can be observed in the time domain. The beginning of the oscillation is dominated by the signal from the SiO₂ layer. After the pulse propagates through the SiO₂, it is back reflected at the interface to the LiNbO₃ layer which can be vaguely observed as a phase shift in the transient at 185 ps. From this point on, both SiO₂ and LiNbO₃ contribute to the signal of the transient, which consists of their time-resolved Brillouin oscillations.

Figure 2a shows the extracted oscillations without the electronic background from the transient of Figure 1. The fast and slow decay components of the background signal mainly stem from electron-phonon scattering and thermal diffusion in the Cr layer, respectively [17–19]. In Figure 2c, the Fast Fourier Transformation (FFT) of the extracted signal of Figure 2a is shown. We present the FFT of the full measurement range because the results obtained for each region separately for the respective

frequency peaks are within the error of 1 GHz. The peak at 20.5 GHz originates from the Brillouin oscillation in SiO₂ and the one at 38.9 GHz from the Brillouin oscillation in LiNbO₃. This allows us to calculate the longitudinal sound velocities v in the respective media by the Brillouin frequencies, which are given by $f = 2nv/\lambda$, with n representing the refractive index in the respective media and λ representing the wavelength of the probe light. For SiO₂, we obtain a longitudinal sound velocity of $v = 5797$ m/s (± 141 m/s) which is in very good agreement with the literature value of 5800 m/s [21]. The uncertainty of the sound velocity takes into account that we have a measurement inaccuracy of the frequency of ± 0.5 GHz. This approach is, however, more complicated in LiNbO₃, as we will discuss in the following. We observe no contribution from the Al layer in our measurements, which would yield a mode at $f = (2n - 1)v/4d = 16$ GHz for $n = 1$ and with the longitudinal sound velocity of Al of $v = 6320$ m/s [22] and the thickness $d = 100$ nm of the Al layer.

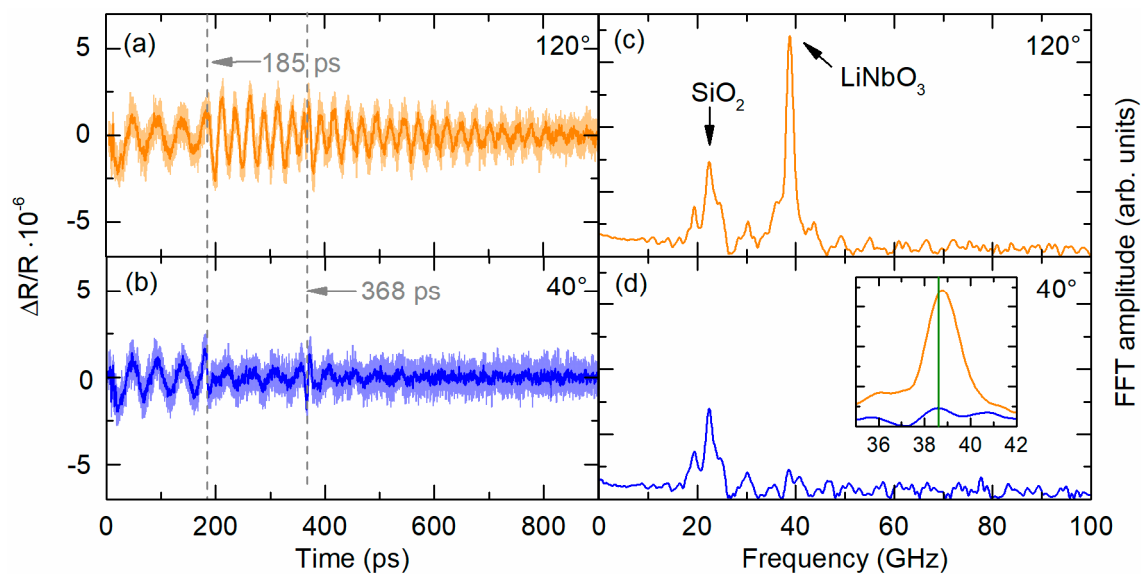


Figure 2. (a,b) Extracted oscillations for different polarization angles; (c,d) respective the Fast Fourier Transformations (FFTs). In the orange graphs, the superimposed response of LiNbO₃ and SiO₂ can be seen (data from the rotation angle of 120° of Figure 3). In the blue graphs, the part of LiNbO₃ is “turned off” (data from the rotation angle of 40° of Figure 3). The inset in (d) shows the shift of the LiNbO₃ frequency for the FFT at 120° and 40°. The green line is a guide to the eye to enable better visibility of the occurring frequency shift.

Recent findings show that the birefringence in LiNbO₃ can give rise to several Brillouin modes which show a distinct dependence on the crystal orientation and the incident probe light polarization, as Lejman et al. showed in Reference [23]. Lejman et al. demonstrate in their work the ultrafast acousto-optic mode conversion induced by coherent acoustic phonons in LiNbO₃. In particular, they observe a strong polarization dependence of the observed Brillouin mode amplitudes caused by different photoelastic constants for their respective polarization orientations. X-ray measurements revealed for our LiNbO₃ layer a crystal orientation of ($\bar{1}14$), which results in a tilt of the crystal of 6.1° against the Z-axis. From this, we can calculate the refractive indices to be $n_o = 2.250$ and $n_e = 2.249$, i.e., almost identical values, for the negative birefringent crystal. Thus, we obtain for the measured frequency $f = 38.9$ GHz in LiNbO₃ a sound velocity of $v = 7090$ m/s (± 90 m/s). We can calculate with the Christoffel equation [24] the expected sound velocities in LiNbO₃ along the ($\bar{1}14$) direction, which are $v_1 = 7245$ m/s for the quasi-longitudinal mode, and $v_{t1} = 3662$ m/s and $v_{t2} = 3540$ m/s for the two quasi-transverse modes. In order to check the possibility of a signal contribution from the transverse components, we also calculate the expected Brillouin frequency of $f \approx 20$ GHz. Indeed, we observe an additional mode close to this frequency in the FFT spectrum displayed in Figure 2. However, an unambiguous assignment is not possible due to the overlap with the SiO₂ mode. We will

show in the following how the polarization-dependent signal detection of the quasi-longitudinal mode can be utilized in our measurements.

Figure 2b,d depict the extracted oscillation and the respective FFT of a measurement of the sample with a different probe pulse polarization (roughly perpendicular polarization with 40° instead of 120° , the 0° polarization angle was chosen arbitrarily). While there is a strong contribution from the LiNbO₃ layer to the time domain signal in Figure 2a, a change in the probe pulse polarization can almost completely suppress it, as evidenced by the signal in Figure 2b and the corresponding FFTs where the respective contributions are marked. This behaviour contains different types of information which we can exploit. If only the contributions from SiO₂ are detected, as in Figure 2b, the discontinuities caused by the acoustic pulse while propagating through the SiO₂/LiNbO₃ interface and the arrival at the sample surface can be clearly identified. This allows us to obtain the time of flight $t = 185$ ps in the SiO₂ layer, which yields (in combination with the earlier calculated sound velocity) the thickness $d = tv = 1072$ nm (± 26 nm) of the SiO₂ layer. Here, we are in excellent agreement with the nominal thickness of $d = 1140$ nm measured with ellipsometry. We want to emphasize at this point that the only a priori knowledge we use for the data evaluation is the index of refraction of the SiO₂ layer, a quantity which is readily available by means of e.g., ellipsometry. Thus, we can obtain the longitudinal sound velocity and the layer thickness simultaneously in one measurement.

It must be pointed out that the features visible in Figure 2b, i.e., the pulses at 185 ps and 368 ps, are already present in Figure 2a, but are hard to distinguish due to the superposition with the LiNbO₃ signal. Here, at 368 ps an acoustic pulse echo after one roundtrip through the SiO₂ becomes visible. To be more precise, the weaker Brillouin oscillation in the SiO₂ can now be observed in the time span from 185 ps to 368 ps. The decrease in amplitude is mainly due to the decrease in the acoustic pulse amplitude caused by the partial transmission of the acoustic pulse into the LiNbO₃ layer. For SiO₂, we cannot obtain any information about the acoustic damping due to the relatively small thickness of the layer. Fits to the experimental data do not reveal a significant decrease in the amplitude. However, the LiNbO₃ layer is thick enough to obtain information on the damping. We obtain a full width at half maximum of 1.56 ± 0.2 GHz from a Lorentzian fit of the corresponding FFT peak, which is consistent to a damping time of 217 ± 20 ps in the time domain obtained by a damped sinusoidal fit. This results in an acoustic absorption coefficient of $\alpha_1 = 4.4 \times 10^3$ cm⁻¹. Compared to the acoustic absorption obtained from the data presented by Lejman et al. in Reference [23], for the Z-cut LiNbO₃ crystal (which is close to our orientation) a considerable decrease in the acoustic absorption is also readily apparent in the time domain measurements, and yields an acoustic absorption coefficient of $\alpha_2 = 2.42 \times 10^3$ cm⁻¹ extracted from the data. The distinct difference may be caused by different film/crystal qualities as well as the fact that our strain pulse is only quasi-longitudinal.

A more detailed look at the probe polarization dependence of the LiNbO₃ signal is shown in Figure 3. The polarization of the probe laser pulse was systematically varied with a half-wave plate. Figure 3 shows the maximum of the amplitude of the FFT resulting from the LiNbO₃ substrate plotted versus the rotation angle of the probe laser pulse polarization.

The peak of the amplitude shows a sinusoidal behaviour with π periodicity fitted to the data points (solid red line) similar to the findings and theoretical considerations in Reference [23]. Here, it is important to note that only the detection sensitivity is influenced. The acoustic pulse still propagates in the LiNbO₃ layer of the sample.

As described in detail in Reference [23] and summarized shortly above, the polarization-dependent elimination of the signal of LiNbO₃ can be explained by the mode conversion process and the polarization-dependent photoelastic constants in the uniaxial birefringent ferroelectric material. Dependent on the LiNbO₃ orientation, probing at normal incidence and in backscattering geometry up to three different Brillouin frequencies can be detected, for ordinary and extraordinary refractive indices as well as a combination of both.

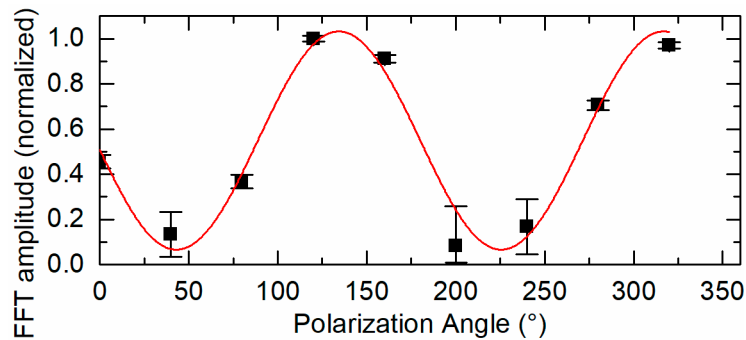


Figure 3. Peak amplitude value of the response of the LiNbO₃ layer plotted as a function of the polarization angle of the incident pulse. The red solid line shows a fit through the experimental data points (black squares) which exhibits a sinusoidal behaviour with π periodicity. The error is estimated by the mean average of the noise floor together with the standard deviation.

This raises the question why we observe only a single Brillouin frequency. In fact, the expected shift for the two polarizations is about 1.4 GHz (as $f_o/f_e = n_o/n_e = 1.037$ for 820 nm) and is thus close to the resolution limit of our system. However, a closer look reveals that we indeed observe a small shift of approximately 0.4 GHz of the Brillouin frequency for orthogonal polarizations, as depicted in the inset in Figure 2d. Nevertheless, with the current system configuration we will not be able to resolve two or three individual modes. This information would indeed be highly desirable to obtain, as the mode occurrence yields information about the LiNbO₃ crystal orientation. It would be possible to improve the results by lowering the probe wavelength to around 400 nm in order to increase the obtained frequency shift and reduce the influence of measurement inaccuracies.

Although we cannot deduce the exact crystal orientation due to the discussed limitations, we can conclude from the pump-probe measurements themselves that the investigated LiNbO₃ layer does not exhibit a Z-cut orientation (001) where the optical axis is perpendicular to the sample surface, because no polarization dependence is expected in this case. Additionally, it is unlikely that the sample shows an X- (100) or Y-cut (010) orientation [25]: comparing the modulation depth in Figure 3 to the results obtained in Reference [23] as well as the observed sound velocities hint to an orientation not identical but close to the Z-axis, which was indeed corroborated by the X-ray measurements.

Furthermore, we want to mention the possibility of obtaining the acoustic reflection coefficient r between the SiO₂ and the LiNbO₃ layer by comparison of the Brillouin amplitudes in Figure 2b before and after the first discontinuity. In this way, we obtain an experimental value of $r = 0.35$. With the earlier determined sound velocities of SiO₂ and LiNbO₃, the reflection coefficient for an assumed perfect interface can be calculated to be $r = (Z_{\text{LiNbO}_3} - Z_{\text{SiO}_2}) / (Z_{\text{LiNbO}_3} + Z_{\text{SiO}_2})$. For our crystal orientation of ($\bar{1}14$) with an acoustic impedance $Z = \rho v$, we can calculate $r = 0.37$. This finding indicates a very good interface adhesion between the respective layers. The small deviation from the reflection coefficient obtained experimentally from the amplitudes can be explained by the measurement inaccuracy. Additionally, it is possible that an interdiffusion at the SiO₂/LiNbO₃ interface appears, which can enhance the acoustic transmission. Indeed, such an interface has been observed in similar layer systems after annealing due to diffusion [26].

4. Conclusions

Time-resolved photoacoustic metrology is applied to characterize SiO₂/LiNbO₃ layer systems. The polarization-dependent detection in LiNbO₃ due to birefringence is utilized to infer information about the sound velocities and film thicknesses, as well as the LiNbO₃ crystal orientation and the layer interface. We show that the possibility to minimize the LiNbO₃ signal contribution by proper choice of the detection pulse polarization can be utilized to obtain more information about the layer structure than is usually possible in similar approaches. This approach is not limited to the layer materials

discussed herein, but can in general increase the feasibility of picosecond ultrasonic measurements in samples where birefringence is present.

Acknowledgments: We would like to thank Evatec AG (Switzerland) as well as Vitalyi Gusev for interesting discussions and Evatec AG for providing the optoacoustic filter samples. We acknowledge the financial support through the Deutsche Forschungsgemeinschaft (SFB 767).

Author Contributions: Mike Hettich, Delia Brick and Thomas Dekorsy conceived and designed the experiments; Delia Brick performed the experiments; Delia Brick, Mike Hettich and Martin Grossmann analyzed the data; Erkan Emre performed the X-ray measurements; Delia Brick and Mike Hettich wrote the manuscript. All authors contributed with discussions.

Conflicts of Interest: The authors declare no conflict of interest. The founding sponsors had no role in the design of the study; in the collection, analyses, or interpretation of data; in the writing of the manuscript, and in the decision to publish the results.

References

1. Ruppel, C.C.; Reindl, L.; Weigel, R. SAW Devices and their Wireless Communication Applications. *IEEE Microw. Mag.* **2002**, *3*, 65–71. [[CrossRef](#)]
2. Lam, C.S. A Review of the Timing and Filtering Technologies in Smartphones. In Proceedings of the IEEE International Frequency Control Symposium, New Orleans, LA, USA, 9–12 May 2016.
3. Thomsen, C.; Grahn, H.T.; Maris, H.J.; Tauc, J. Surface generation and detection of photons by picosecond light pulses. *Phys. Rev.* **1986**, *34*, 4129–4138. [[CrossRef](#)]
4. Thomsen, C.; Strait, J.; Vardeny, Z.; Maris, H.J.; Tauc, J.; Hauser, J.J. Coherent phonon generation and detection by picosecond light pulses. *Phys. Rev. Lett.* **1984**, *53*, 989–992. [[CrossRef](#)]
5. Mante, P.A.; Robillard, J.F.; Devos, A. Complete thin film mechanical characterization using picosecond ultrasonics and nanostructured transducers: Experimental demonstration on SiO₂. *Appl. Phys. Lett.* **2008**, *93*, 1–4. [[CrossRef](#)]
6. Mounier, D.; Morozov, E.; Ruello, P.; Breteau, J.; Picart, P.; Gusev, V. Detection of shear picosecond acoustic pulses by transient femtosecond polarimetry. *Eur. Phys. J. Spec. Top.* **2008**, *153*, 243–246. [[CrossRef](#)]
7. Pezeril, T.; Chigarev, N.; Ruello, P.; Gougeon, S.; Mounier, D.; Breteau, J.; Picart, P.; Gusev, V. Laser acoustics with picosecond collimated shear strain beams in single crystals and polycrystalline materials. *Phys. Rev. B* **2006**, *73*, 132301. [[CrossRef](#)]
8. Mounier, D.; Morosov, E.; Ruello, P.; Edely, M.; Babilotte, P.; Mechri, C.; Breteau, J.-M.; Gusev, V. Application of transient femtosecond polarimetry/ellipsometry technique in picosecond laser ultrasonics. *J. Phys. Conf. Ser.* **2007**, *92*, 12179. [[CrossRef](#)]
9. Weber, M.F.; Stover, C.A.; Gilbert, L.R.; Nevitt, T.J.; Ouderkirk, A.J. Giant Birefringent Optics in Multilayer Polymer Mirrors. *Science* **2000**, *287*, 2451–2456. [[CrossRef](#)] [[PubMed](#)]
10. Reyes-Esqueda, J.A.; Torres-Torres, C.; Cheang-Wong, J.C.; Crespo-Sosa, A.; Rodríguez-Fernández, L.; Noguez, C.; Oliver, A. Large optical birefringence by anisotropic silver nanocomposites. *Opt. Express* **2008**, *16*, 710–717. [[CrossRef](#)] [[PubMed](#)]
11. Harris, B.K.D.; van Popta, A.C.; Sit, J.C.; Broer, D.J.; Brett, M.J. A Birefringent and Transparent Electrical Conductor. *Adv. Funct. Mater.* **2008**, *18*, 2147–2153. [[CrossRef](#)]
12. Muskens, O.L.; Borgström, M.T.; Bakkers, E.P.A.M.; Rivas, J.G. Giant optical birefringence in ensembles of semiconductor nanowires. *Appl. Phys. Lett.* **2006**, *89*, 233117. [[CrossRef](#)]
13. Künzner, N.; Kovalev, D.; Diener, J.; Gross, E.; Timoshenko, V.Y.; Polisski, G.; Koch, F. Giant birefringence in anisotropically nanostructured silicon. *Opt. Lett.* **2001**, *26*, 1265–1267. [[CrossRef](#)] [[PubMed](#)]
14. Ristow, O.; Merklein, M.; Grossmann, M.; Hettich, M.; Schubert, M.; Bruchhausen, A.; Grebing, J.; Erbe, A.; Mounier, D.; Gusev, V.; et al. Ultrafast spectroscopy of super high frequency mechanical modes of doubly clamped beams. *Appl. Phys. Lett.* **2013**, *103*, 233114. [[CrossRef](#)]
15. Bartels, A.; Cerna, R.; Kistner, C.; Thoma, A.; Hudert, F.; Janke, C.; Dekorsy, T. Ultrafast time-domain spectroscopy based on high-speed asynchronous optical sampling. *Rev. Sci. Instrum.* **2007**, *78*, 35107. [[CrossRef](#)] [[PubMed](#)]
16. Gebs, R.; Klatt, G.; Janke, C.; Dekorsy, T.; Bartels, A. High-speed asynchronous optical sampling with sub-50fs time resolution. *Opt. Express* **2010**, *18*, 5974–5983. [[CrossRef](#)] [[PubMed](#)]

17. Saito, T.; Matsuda, O.; Wright, O.B. Picosecond acoustic phonon pulse generation in nickel and chromium. *Phys. Rev. B* **2003**, *67*, 205421. [[CrossRef](#)]
18. Ruello, P.; Gusev, V.E. Physical mechanisms of coherent acoustic phonons generation by ultrafast laser action. *Ultrasonics* **2014**, *56*, 21–35. [[CrossRef](#)] [[PubMed](#)]
19. Fujimoto, J.G.; Liu, J.M.; Ippen, E.P.; Bloembergen, N. Femtosecond Laser Interaction with Metallic Tungsten and Nonequilibrium Electron and Lattice Temperatures. *Phys. Rev. Lett.* **1984**, *53*, 1837–1840. [[CrossRef](#)]
20. Devos, A. Colored ultrafast acoustics: From fundamentals to applications. *Ultrasonics* **2015**, *56*, 90–97. [[CrossRef](#)] [[PubMed](#)]
21. Nazaretski, E.; Merithew, R.D.; Pohl, R.O.; Parpia, J.M. Measurement of the acoustic properties of amorphous silica above 4.5 mK. *Phys. Rev. B* **2005**, *71*, 144201. [[CrossRef](#)]
22. Chern, E.J.; Nielsen, H.T.C. Generalized formulas for reflected pulse response of multilayered structures. *J. Appl. Mech.* **1989**, *66*, 2833. [[CrossRef](#)]
23. Lejman, M.; Vaudel, G.; Infante, I.C.; Chaban, I.; Pezeril, T.; Edely, M.; Nataf, G.F.; Guennou, M.; Kreisel, J.; Gusev, V.E.; et al. Ultrafast acousto-optic mode conversion in optically birefringent ferroelectrics. *Nat. Commun.* **2016**, *7*. [[CrossRef](#)] [[PubMed](#)]
24. Auld, B.A. *Acoustic Fields and Waves in Solids*; Wiley: New York, NY, USA, 1973.
25. MTI Corporation. Available online: <http://www.mtixtl.com/linbo3.aspx> (accessed on 15 April 2017).
26. Nagata, H.; Takahashi, H.; Takai, H.; Kougo, T. Impurity Evaluations of SiO₂ Films Formed on LiNbO₃ Substrates. *Jpn. J. Appl. Phys.* **1995**, *34*, 606–609. [[CrossRef](#)]



© 2017 by the authors. Licensee MDPI, Basel, Switzerland. This article is an open access article distributed under the terms and conditions of the Creative Commons Attribution (CC BY) license (<http://creativecommons.org/licenses/by/4.0/>).